Chemical Science

ROYAL SOCIETY OF CHEMISTRY

EDGE ARTICLE

View Article Online
View Journal | View Issue

Cite this: *Chem. Sci.*, 2025, **16**, 23077

All publication charges for this article have been paid for by the Royal Society of Chemistry

Rigid-flexible coupling: exquisite modulation of asymmetrical spiro-type hole-transporting materials toward efficient and stable perovskite solar cells

Xuran Wang,[a] Jihong Wu,[a] Guosen Zhang,[a] Ruidan Zhang,[a] Mingwei An, *[a] Xiafeng He,[a] Xiaozhen Huang,[a] Jie Gao,[a] Hongfang Du, [a] Yue Wang, [a] Dong Wei, *[a] Daqin Chen, *[a] Yang Wang *[ab] and Wei Huang*[acd]

Received 25th July 2025
Accepted 24th October 2025

DOI: 10.1039/d5sc05563f

rsc.li/chemical-science

Hole-transporting materials (HTMs) are the cornerstone to ensure efficient charge extraction and transport in conventional perovskite solar cells (PSCs). Despite the development of numerous novel HTMs, their performance consistently lags behind that of the benchmark, Spiro-OMeTAD. However, the instability of Spiro-OMeTAD induced by heavy doping remains a critical limitation. Herein, based on a Spiro-type molecular skeleton, we design a series of HTMs (namely 3MPA, 2MPA, MPA, and 4MCz) by precisely regulating the peripheral flexible diphenylamine and rigid carbazole fragments, which enables synergistic modulation of multiple properties of the HTMs. Specifically, the introduction of more carbazole units leads to enhanced thermal stability, lowered HOMO energy level, more compact film morphology and strengthened passivation capacity, but inversely, decreased solubility, doping efficiency and conductivity of the HTMs. Consequently, 3MPA and 2MPA can enable high-performance PSCs at low doping concentrations with PCEs of 25.21% and 24.86%, respectively, and importantly, 2MPA based PSCs exhibit superior device stability under ISOS-D-1 and ISOS-D-2 conditions.

Introduction

Perovskite solar cells (PSCs) have garnered great interest as a third-generation photovoltaic technique over the past decade due to their low-cost processing and stepwise breakthrough in power conversion efficiencies (PCEs) which have witnessed a certified value above 26%.[1–4] In the components of PSCs, the hole-transporting materials (HTMs) play vital roles in extracting and transporting holes, blocking electrons and protecting perovskite layers against oxygen and moisture, especially for n-i-p structured PSCs where 2,2′,7,7′-tetrakis(*N*,*N*-di-*p*-methoxyphenylamino)-9,9′-spirobifluorene(Spiro-OMeTAD, abbreviated as Spiro) is the dominant HTM owing to its commercial availability and application universality.[5–9] However, Spiro suffers low intrinsic hole mobility and needs additional dopants to enhance conductivity which may in turn reduce device stability.[10,11] Moreover, Spiro shows poor molecular packing which requires a high concentration of HTM solutions to ensure dense and pinhole-free films. This may increase the material consumption and preparation cost.[12,13]

To boost the durability of HTMs and the operational stability of PSCs, various chemical design strategies, including conjugation extension,[14,15] donor–acceptor framework,[16,17] conformational lock design,[18,19] dendrimer construction[20] and side-chain engineering, have been put forward to strengthen the intermolecular interactions and optimize the aggregation behavior in the solid state which is conducive to enhancing the hole mobility and film morphological properties of HTMs.[21–24] However, regardless of the strategy adopted, diphenylamine and carbazole as the classical hole-transporting building blocks are commonly integrated into the molecular structure. Both of them feature similar chemical compositions and readily available raw materials but distinct characteristics. Generally, diphenylamine is more easily oxidized, thereby facilitating the generation of more hole carriers. However, the flexibility of diphenylamine may inhibit the ordered stacking of molecules and reduce thermal stability. In comparison, carbazole features a planar and rigid structure which is

[a]*Strait Institute of Flexible Electronics (SIFE, Future Technologies), College of Physics and Energy, Fujian Key Laboratory of Flexible Electronics, Fujian Provincial Key Laboratory of Quantum Manipulation and New Energy Materials, Fujian Normal University, Strait Laboratory of Flexible Electronics (SLoFE), Fuzhou 350117, Fujian, China. E-mail: ifemwan@fjnu.edu.cn; q397983012@126.com; dqchen@fjnu.edu.cn; ifewangy@fjnu.edu.cn; vc@nwpu.edu.cn*

[b]*State Key Laboratory of Structural Chemistry, Fujian Institute of Research on the Structure of Matter, Chinese Academy of Sciences, Fuzhou, Fujian 350002, China*

[c]*Frontiers Science Center for Flexible Electronics (FSCFE), MIIT Key Laboratory of Flexible Electronics (KLoFE), Northwestern Polytechnical University, Xi'an 710072, China*

[d]*State Key Laboratory of Flexible Electronics (LoFE), Institute of Advanced Materials (IAM), School of Flexible Electronics (Future Technologies), Nanjing Tech University (NanjingTech), Nanjing 210003, Jiangsu, China*

beneficial for enhancing molecular packing and improving thermal stability, whereas the disadvantages lie in its inferior oxidative capacity and deep-lying energy level. Despite the ample variety of HTMs involving diphenylamine or carbazole, few studies have focused on the specific structure–property relationships induced by the discrepancy in two building blocks. In fact, it is challenging to precisely elucidate the subtle influences of diphenylamine and carbazole on the properties of HTMs due to quite different molecular structures reported in the literature.[25–31]

Recently, an anisotropic regulation strategy was proposed by our group through constructing diphenylamine/carbazole-containing HTMs based on the high chemoselectivity of the spiro-skeleton.[32] It was found that with the same spiro-skeleton, replacing half of the flexible diphenylamine units with rigid carbazole units can profoundly alter the electrical properties, film morphologies and interfacial charge dynamics of the HTMs. Hence, in this work, by further exquisitely adjusting the ratio of diphenylamine to carbazole in Spiro, more insight into the effect of the spatial structure of spiro-type HTMs on the structure–property–performance correlations could be systematically rationalized. Specifically, based on the Spiro molecule, a carbazole unit was introduced to replace the diphenylamine unit one by one, forming 7′-(3,6-dimethoxy-9*H*-carbazol-9-yl)-2,2,7-tris(*N*,*N*-di-*p*-methoxyphenylamino)-9,9′-spirobifluorene (denoted as 3MPA), 2′,7′-(3,6-dimethoxy-9*H*-carbazol-9-yl)-2,7-bis(*N*,*N*-di-*p*-methoxyphenylamino)-9,9′-spirobifluorene (denoted as 2MPA), 2′,7,7′-(3,6-dimethoxy-9*H*-carbazol-9-yl)-2-bis(*N*,*N*-di-*p*-methoxyphenylamino)-9,9′-spirobifluorene (denoted as MPA), and 2,2′,7,7′-tetrakis(3,6-dimethoxy-9*H*-carbazol-9-yl)-9,9′-spirobifluorene (denoted as 4MCz), respectively. Interestingly, it was found that as the proportion of rigid carbazole units increases, the resultant HTMs exhibit elevated thermal stability and lowered energy levels as well as more compact molecular packing and a denser thin film. However, the solubility of HTMs decreases especially for 4MCz due to excessive rigid carbazole units. Also, the doping efficiency and the resultant film conductivity deteriorate owing to the reduction of oxidation-active diphenylamine groups. Leveraging the synergistic modulation of HTM properties by meticulous combination of flexible diphenylamine units and rigid carbazole moieties, the 3MPA and 2MPA based PSCs can deliver high performance at low doping concentrations with PCEs of 25.21% and 24.86%, respectively. More importantly, 2MPA based devices show superior stability under ISOS-D-1 (>2000 h) and ISOS-D-2 (>550 h) protocol aging tests with over 80% of initial efficiency remaining. These results highlight the critical role of flexible and rigid building blocks in governing the multifaceted properties of HTMs and establish clear correlations between molecular structure, material properties and device performance, which may offer valuable guidelines for the design of efficient and stable HTMs applied in PSCs.

Results and discussion

Molecular synthesis and characterization

The synthesis of all spiro-type HTMs presented in this work is depicted in Fig. 1a. By utilizing 2,7-dibromo-2′,7′-diiodo-9,9′-spirobi[fluorene] as the key intermediate, SF-MPA-Br and SF-MCz-Br can be selectively obtained in decent yield above 50%. Subsequently, Buchwald coupling with bis(4-methoxyphenyl) amine and 3,6-dimethoxy-9*H*-carbazole in a 1 : 1 : 1 molar ratio *via* a one-pot procedure can produce 3MPA and MPA in moderate yields of 27% and 33%, respectively. The synthesis of Spiro and 2MPA follows the synthetic route described in the previous work,[32,33] while 4MCz can be afforded using the same method as Spiro in a high yield of 79%. The chemical structures of the novel HTMs 3MPA, MPA and 4MCz were well characterized by ^{1}H nuclear magnetic resonance (NMR), ^{13}C NMR and matrix-assisted laser desorption ionization time-of-flight (MALDI-TOF) mass spectrometry (Fig. S1–S10). It was found that the molecular polarity increases with the growing number of carbazole units as shown in thin-layer chromatography (Fig. S11a). The fundamental DFT calculations, including electrostatic potential (ESP) mapping and frontier molecular orbitals (HOMO and LUMO), as well as reorganization energy have been provided in Fig. S12 and Table S1. Collectively, the increment of carbazole units enhances the electron-rich regions of the molecule, lowers the HOMO energy level, and reduces the reorganization energy, indicating improved hole transport capacity. The solubility of the HTMs is not varied except for 4MCz which shows extremely low solubility in chlorobenzene ($\sim$3 mg mL^{-1}) probably due to its highly rigid molecular structure (Fig. S11b). This is clearly unfavorable for solution processing and the formation of a sufficiently thick hole-transporting layer (HTL) in n-i-p PSCs. Regarding the aggregation behavior in solution, we performed dynamic light scattering (DLS) measurements of HTMs as shown in Fig. S13. Clearly, as the number of carbazole units increases, the particle size of HTMs in solution gradually enlarges, which can be attributed to enhanced molecular aggregation from Spiro to MPA.

The thermal stability of the HTMs was characterized using thermogravimetry analysis (TGA) and differential scanning calorimetry (DSC) as shown in Fig. 1b and c. Obviously, the decomposition temperature (T_d) gradually rises from 438 °C (Spiro) to 460 °C (4MCz) with the increasing number of carbazole moieties (Table 1). Similarly, the glass transition temperature (T_g) also shows an increase from 121 °C for Spiro to 172 °C for MPA, indicating improved thermal stability after incorporating more rigid carbazole units (Table 1).

Fluorescence anisotropy was employed to study the symmetry of HTMs (Fig. 1d). The anisotropy (r) value can be obtained following the previous work (Table 1). Compared to low r of highly symmetrical Spiro (0.005) reported in the literature,[34] 2MPA, 3MPA and MPA show gradually increased r of 0.0098, 0.0115 and 0.0148, respectively, due to the growing asymmetry of HTMs.

Optoelectronic properties and film morphology

The UV-vis absorption spectra were measured to reveal the optical properties of spiro-type HTMs. As exhibited in Fig. 1e, all of the HTMs show double absorption peaks in solutions where the absorption peaks at 300 to 350 nm are assigned to the π–π* transition while those in the range of 350–400 nm are attributed

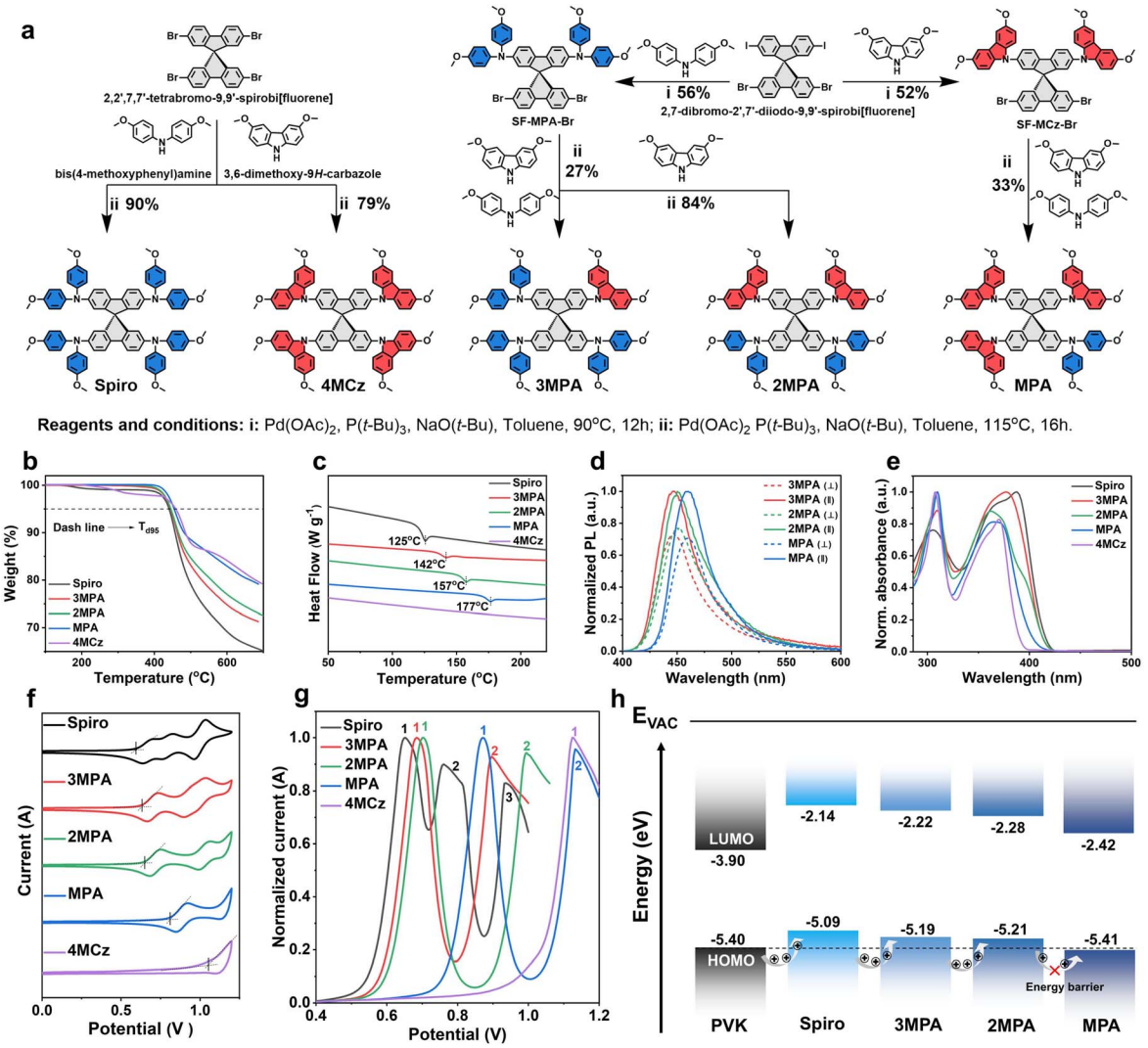

Fig. 1 Molecular synthesis routes and basic optoelectronic and thermal properties. (a) Synthetic routes for HTMs. (b) TGA curves of HTMs. (c) DSC curves of HTMs, the vertical dashed lines indicate the glass transition temperature. (d) Fluorescence anisotropy of 3MPA, 2MPA and MPA. (e) Normalized UV-vis absorption spectra of HTMs in solution. (f) Cyclic voltammograms and (g) DPV curves of HTMs in solution. (h) Energy level alignment schematics of the perovskite and HTMs.

to the charge transfer (CT) transition from the peripheral fragments to the central spirofluorene. On going from the solution state to film state, Spiro and 3MPA show identical absorption profiles while 2MPA and MPA exhibit an obvious redshift of ~10 nm (Fig. S14), indicating the tendency to aggregate with the increasing number of carbazole units. The variation of aggregation behavior will significantly affect the film morphological properties of HTMs as will be discussed later.

Cyclic voltammetry (CV) was employed to evaluate the highest occupied molecular orbital (HOMO) energy levels of the HTMs in solutions. As shown in Fig. 1f, Spiro undergoes three successive oxidation processes derived from diphenylamine units, leading to monocationic, dicationic and tricationic radicals, respectively, which is consistent with the results in the literature.[35] With the introduction of more carbazole units, the first oxidation wave moves gradually to high potential from 3MPA to MPA along with the reduction of oxidation processes. This is attributed to the relatively low oxidative activity of carbazole as can be found in the CV curve of 4MCz which possesses much higher oxidation potential than Spiro. To further elucidate this observation, differential pulse voltammetry (DPV) was conducted as exhibited in Fig. 1g and S15. Clearly, the incorporation of carbazole units may shift the oxidation potential to higher values especially for MPA due to the direct electronic coupling between carbazole and diphenylamine *via* the conjugated fluorene spacer (Fig. S16). Hence, the HOMO levels are gradually lowered from Spiro (−5.11 eV) to 3MPA (−5.15 eV), 2MPA (−5.17 eV) and MPA (−5.34 eV). Note that the HOMO level of 4MCz (−5.58 eV) is too deep to provide sufficient driving force for hole transfer.[36] To gain more insight into the molecular energetics, ultraviolet photoelectron spectroscopy (UPS) was performed to detect the energy levels of HTMs in the film state. By analyzing the cutoff (E_{cutoff}) and onset (E_{onset}) energy regions in the spectra in Fig. S17, the HOMO levels are calculated to be −5.09, −5.19, −5.21 and −5.41 eV for Spiro, 3MPA, 2MPA and MPA, respectively, showing the

Table 1 Optical, electrochemical and thermal properties of HTMs and the corresponding electrical properties[a]

Compounds	λ_{max} (nm)		λ_{onset} (nm)									
	Solution	Film	Film	E_g^{opt} (eV)	E_{HOMO}^{DPV} (eV)	E_{HOMO}^{UPS} (eV)	E_{LUMO}^{opt} (eV)	T_g (°C)	T_{d95} (°C)	r	Hole mobility ($cm^2 V^{-1} s^{-1}$)	Conductivity ($S cm^{-1}$)
Spiro	385	386	416	2.95	−5.11	−5.09	−2.14	125	438	0.005	1.58×10^{-4}	6.86×10^{-6}
3MPA	376	377	417	2.97	−5.15	−5.19	−2.22	142	443	0.0115	1.95×10^{-4}	9.90×10^{-6}
2MPA	363	374	423	2.93	−5.17	−5.21	−2.28	157	446	0.0098	2.34×10^{-4}	7.47×10^{-6}
MPA	362	376	413	2.99	−5.34	−5.41	−2.41	177	453	0.0148	2.40×10^{-4}	2.57×10^{-6}
4MCz	370	—	—	3.19	−5.58	—	—	—	460	—	—	—

[a] $E_g^{opt} = 1240/\lambda_{onset}$ (Film state). $E_{HOMO}^{DPV} = -(E_{ox} + 5.1)$ eV, where Fc/Fc$^+$ *vs.* vacuum = −5.1 eV, E_{ox} is the first oxidation peak of $E_{1/2,ox}$ (V *vs.* Fc/Fc$^+$), and the $E_{1/2,ox}$ of Fc/Fc$^+$ is located at 0.636 V. $E_{HOMO}^{UPS} = E_v = h\nu - (E_{cutoff} - E_{onset})$, where the value of $h\nu$ is 21.22 eV. $E_{LUMO}^{opt} = (E_{HOMO}^{UPS} + E_g^{opt})$.

consistent variation trend with the measurements in solutions. Compared to the valence band maximum (VBM) of the perovskite used in this work (−5.40 eV), 3MPA and 2MPA feature better energy level alignment which is conducive to hole transfer between the perovskite and HTL (Fig. 1h).

Apart from energy level alignment, film morphology is equally crucial, which may affect various properties such as interfacial contact, hole mobility and conductivity, doping characteristics and ion migration. Given that 4MCz suffers from poor solubility and film-forming properties, we excluded it from the subsequent morphological characterizations. First, atomic force microscopy (AFM) was carried out to analyze the surface morphology of HTM films. As shown in Fig. S18, with the increasing number of carbazole units, the HTM films exhibit a pronounced aggregated surface morphology, which is consistent with the UV-vis absorption results. This is accompanied by the increment in root-mean-square (RMS) surface roughness from Spiro (1.79 nm) to MPA (4.02 nm). Subsequent water contact angle measurements further reveal that the HTM films become more hydrophobic as the number of carbazole units increases (Fig. S19). Further, two-dimensional (2D) grazing incidence wide-angle X-ray scattering (2D-GIWAXS) was employed to investigate the molecular packing of HTMs in bulk thin films. As can be seen from the diffraction patterns (Fig. 2a–d), all of the HTMs display ring-shaped diffraction halos, indicative of their amorphous nature. However, Spiro and 3MPA exhibit obviously stronger (010) diffraction signals compared to 2MPA and MPA, which can also be confirmed from the narrower full width at half maximum (FWHM) in the one-dimensional (1D) plots (Fig. S20). This suggests that Spiro and 3MPA may feature more extensive π–π stacking regions than 2MPA and MPA in thin films. Nevertheless, the π–π stacking distances of 2MPA (4.87 Å) and MPA (4.86 Å) are calculated to be shorter than those of Spiro (4.94 Å) and 3MPA (4.91 Å) (Table S2), which implies that increasing the number of carbazole units can lead to more compact molecular packing despite of fewer distinct π–π stacking domains. Such overall tight molecular packing in bulk film is conducive to the enhancement of hole mobility in the pristine film as can be seen in the space-charge-limiting-current (SCLC) measurements (Fig. S21), showing higher hole mobilities for 2MPA (2.34×10^{-4} cm^2 V^{-1} s^{-1}) and MPA (2.40×10^{-4} cm^2 V^{-1} s^{-1}) than Spiro (1.58×10^{-4} cm^2 V^{-1} s^{-1}) and 3MPA (1.95×10^{-4} cm^2 V^{-1} s^{-1}).

As the doping strategy is usually adopted to improve the conductivity of HTMs, we conducted the characterizations of the doped HTM films. Notably, the doping concentration may significantly affect the doping efficiency, film morphology, and the ultimate device performance. Therefore, we used the optimal doping concentration of lithium bis(trifluoromethanesulphonyl)imide (Li-TFSI) (∼55% mol for Spiro, ∼45% mol for 3MPA, ∼35% mol for 2MPA, and ∼100% mol for MPA), which is determined from the best-performing devices to investigate the properties of HTM films (Fig. S22). First, AFM measurements were performed as shown in Fig. 2e–h. The doped Spiro film displays a pronounced pinhole-rich microstructure with high R_{RMS} of 9.78 nm. When the rigid carbazole unit is introduced, the pinhole-like structure

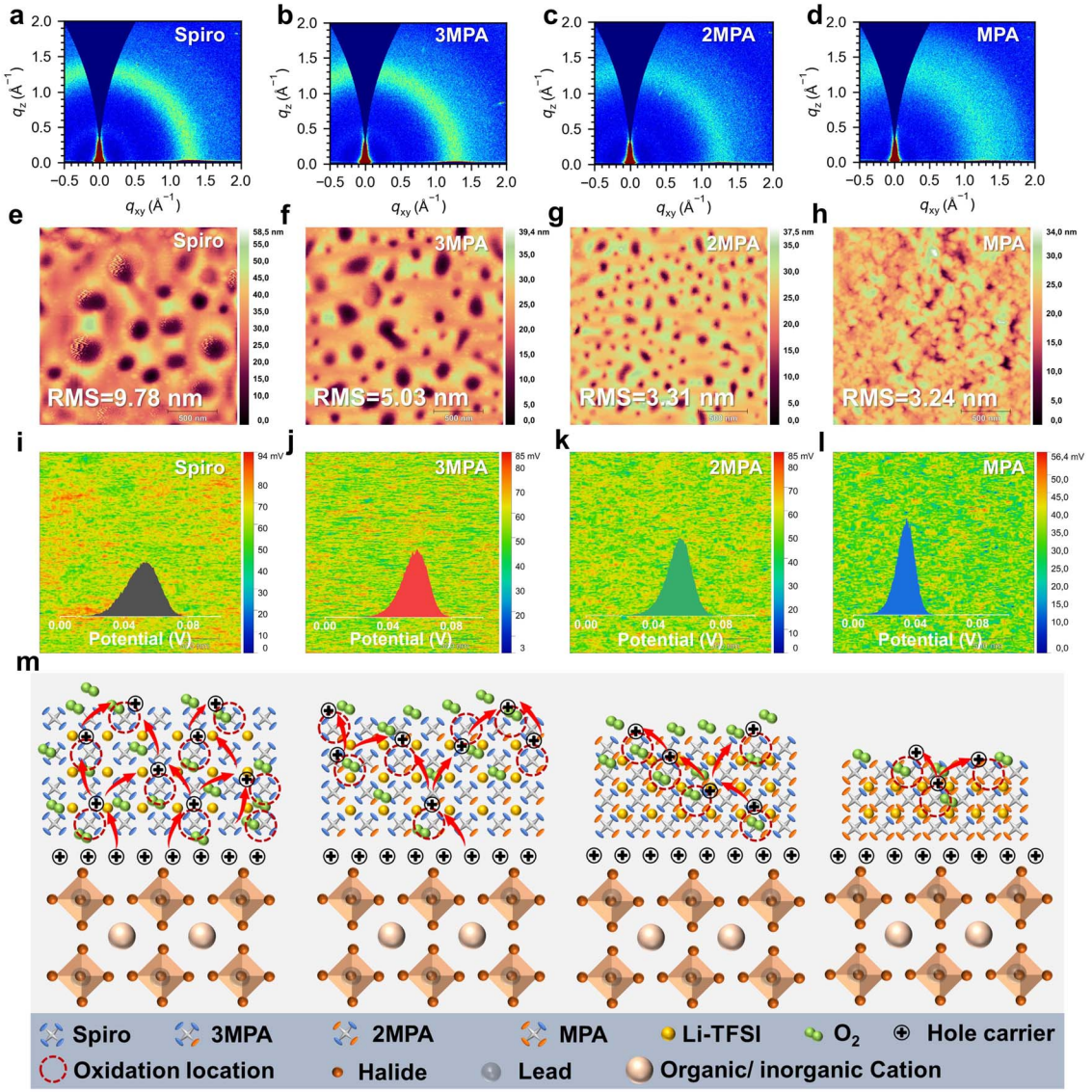

Fig. 2 Molecular packing and surface morphology. (a–d) Two-dimensional (2D) GIWAXS patterns of HTM films deposited on silicon substrates. (e–h) The tapping-mode AFM morphological height images of doped HTM films deposited on FTO substrates. (i–l) Corresponding KPFM images and CPD distribution (inside) of doped HTM films. (m) Schematic illustration of HTM films with the oxygen-induced doping process.

becomes smaller for 3MPA with remarkably reduced R_{RMS} of 5.03 nm. By further increasing the number of carbazole units, the porosity of the doped films is progressively suppressed for 2MPA and MPA, indicating more compact films of the doped HTMs. Similarly, Kelvin probe force microscopy (KPFM) was conducted to study the surface morphology of doped films with contacting potential difference (CPD) images shown in Fig. 2i–l. Apparently, a narrower variation in CPD values is observed with reduced full width at half maximum (FWHM) from Spiro (FWHM ≈ 23.7 mV) to MPA (FWHM ≈ 13.4 mV), implying the uniform and dense films of HTMs with more carbazole units.

To gain insight into the doping behavior of different HTMs, we measured the UV-visible absorption spectra of HTM films with varied doping concentrations. Note that lithium salt doping is closely related to the oxidation time. Hence, for fair comparison, we measured the saturation oxidation time for each HTM, which was approximately found to be 5, 7, 10, and 14 days for Spiro, 3MPA, 2MPA and MPA, respectively. As shown in Fig. S23, a pronounced absorption peak at 520 nm was observed for Spiro which is ascribed to the absorption of the mono-cationic radical of Spiro (abbreviated as Spiro$^{\bullet+}$) as confirmed in the literature.[37]

As the dopant content increases, the absorption peak at 520 nm is strengthened due to the increment of Spiro$^{\bullet+}$ which means a rise in hole carrier concentration. Interestingly, for 3MPA and 2MPA, the absorption peak at 520 nm, corresponding to 3MPA$^{\bullet+}$ and 2MPA$^{\bullet+}$, can reach a near-saturation value with the increase of doping concentration, indicating that a relatively high doping efficiency can be achieved even at lower doping concentrations and this trend was quantitatively characterized by calculating the "standardized absorptance ratio" (SAR) value (Table S3).[37] Meanwhile, for MPA, the

characteristic absorption peak of $MPA^{\bullet+}$ exhibits a redshift to 760 nm, which may be due to different electronic coupling interactions between the diphenylamine/diphenylamine radical and carbazole/diphenylamine radical as illustrated in Fig. S23. Also, the absorption intensity of $MPA^{\bullet+}$ remains relatively weak and shows negligible variation across a wide doping concentration range, which suggests relatively low doping efficiency.

Since doping efficiency directly determines the hole carrier concentration, which is intrinsically linked to film conductivity, we measured the electrical conductivity of the doped HTMs. As displayed in Fig. S24, 3MPA shows the highest conductivity of 9.90×10^{-6} S cm^{-1}, followed by 2MPA (7.47×10^{-6} S cm^{-1}), Spiro (6.86×10^{-6} S cm^{-1}) and MPA (2.57×10^{-6} S cm^{-1}). By comparing the film morphology, hole mobility, doping behavior, and electrical conductivity of all the HTMs, we speculate that the increasing number of carbazole units may enhance the compactness of film morphology, thereby promoting hole mobility. Conversely, the reduced diphenylamine units would negate the oxidation efficiency of HTMs. Simultaneously, the denser film morphology may retard oxygen penetration, thereby affecting doping efficiency (Fig. 2m). Therefore, the HTMs with fewer diphenylamine groups may suffer low hole carrier concentration under saturated doping concentration, which lead to the higher conductivity of 3MPA and 2MPA compared to Spiro and MPA.

Interfacial interactions and carrier dynamics

To gain deep insight into the interfacial interactions between perovskite and different HTMs and the related interfacial carrier dynamics, X-ray photoelectron spectroscopy (XPS) was first employed by depositing thin films of pure HTMs on the perovskite surface to exclude any influence from dopants. As shown in Fig. 3a, the Pb 4f signals of the perovskite shift to a lower binding energy after coating with Spiro and 3MPA. Interestingly, as the number of carbazole units increases, the Pb peaks shift further toward lower binding energy for 2MPA and MPA. This is probably because the rigid carbazole units can stabilize the molecular framework and enable stronger anchoring to the perovskite surface, which is conducive to enhance the interactions with Pb vacancies on the perovskite surface.[32] To further elucidate the role of O/N-donor sites in interacting with Pb^{2+}, XPS measurements of the O 1s and N 1s spectra were performed as exhibited in Fig. S25. The O 1s peaks of 2MPA and MPA exhibit pronounced shifts toward higher binding energies after deposition on the perovskite, in sharp contrast to the negligible changes observed for Spiro and 3MPA. In comparison, the N 1s peaks show almost no discernible shifts for all the HTMs before and after depositing on the perovskite, which can be attributed to steric hindrance that

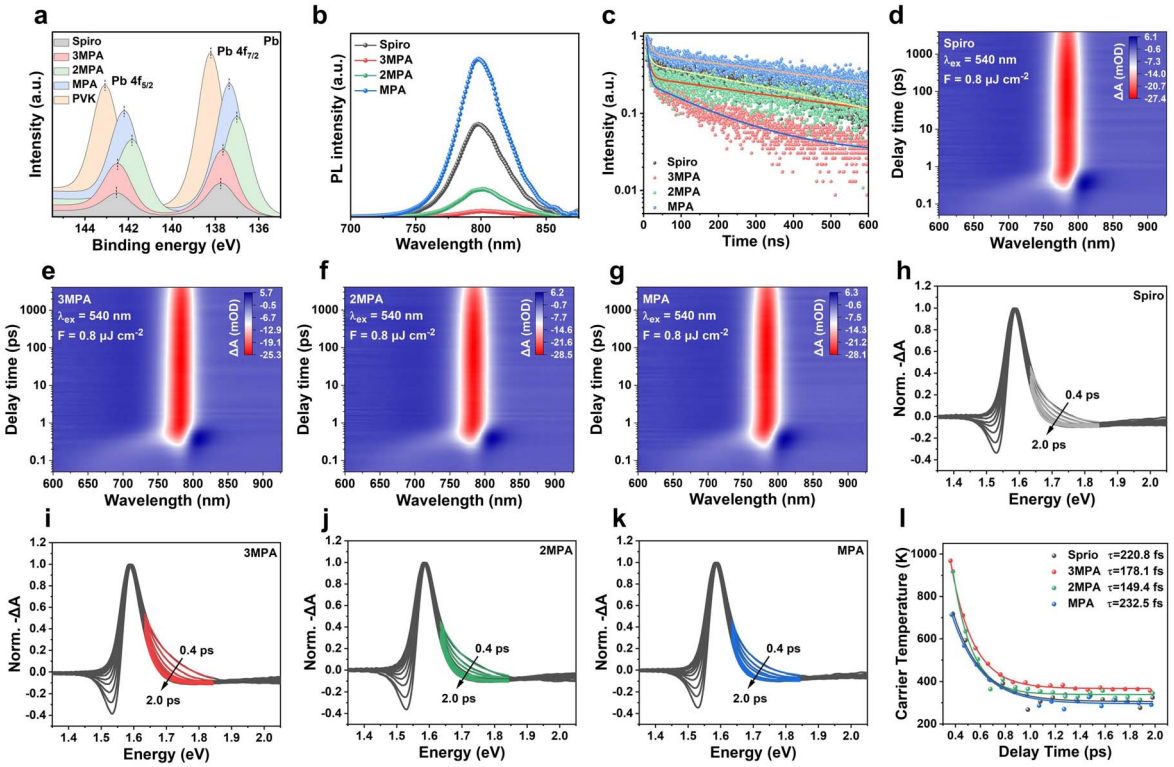

Fig. 3 Interfacial interactions and carrier dynamics. (a) Pb 4f XPS spectra of the pristine perovskite film and those treated with different HTMs. (b) Steady-state PL spectra and (c) time-resolved PL spectra of perovskite films coated with different HTMs. (d–g) 2D pseudo-color plots of the fs-TA spectrum with different perovskite/HTMs. (h–k) The normalized TA spectral profiles. High energy tails in the range of 1.63 to 1.85 eV are fitted by a Maxwell–Boltzmann distribution (color lines) to extract T_c. (l) Time-dependent T_c for both samples. Curves are offset vertically by 100 K sequentially for clarity.

impedes the interaction between N atoms and Pb^{2+} at the interface. These results indicate that the methoxy groups in 2MPA and MPA possess a stronger affinity toward under-coordinated Pb vacancies,[38] thereby reinforcing their passivation capacity at the perovskite interface.

To further substantiate this conclusion, ATR-FTIR measurements were conducted to probe the interactions between the perovskite and HTMs (Fig. S26). Distinct absorption features can be identified at ~1203 cm^{-1} (carbazole CH–O) and ~1236 cm^{-1} (diphenylamine CH–O), revealing clear differences in interaction strength. Notably, 2MPA exhibits the largest wavenumber shift, followed by MPA and 3MPA, whereas Spiro shows negligible changes. These results are fully consistent with the XPS findings, demonstrating that the incorporation of carbazole units may lead to stronger interfacial interactions and more effective defect passivation.

Subsequently, photoluminescence (PL) and time-resolved photoluminescence (TRPL) measurements were conducted to evaluate interfacial charge dynamics. As illustrated in Fig. 3b, the perovskite film covered with 3MPA exhibits the lowest PL intensity, followed by 2MPA, Spiro and MPA. Since the PL quenching is governed by the competition between charge extraction and charge recombination processes, TRPL measurement is utilized to carefully probe interfacial charge dynamics. As displayed in Fig. 3c and Table S4, all of the PL decay curves exhibit biexponential lifetimes with an initial fast decay (τ_1) and second slow decay (τ_2), corresponding to charge extraction and recombination processes, respectively.[39] Apparently, 3MPA treated perovskite has the shortest τ_1 (4.99 ns) and τ_2 (170.38 ns), implying the fastest charge extraction rate and relatively severe charge recombination. With the increment of carbazole units, the charge extraction capacity is weakened with prolonged τ_1 from 7.29 ns for 2MPA to 12.19 ns for MPA which may be due to the mismatched energy level between the perovskite and HTMs. Meanwhile, the τ_2 enhancement from 2MPA (524.77 ns) to MPA (767.24 ns) means that charge recombination is inhibited to some extent which is probably owing to the improved passivation capacity between perovskite and HTMs as previously confirmed.

Transient absorption spectroscopy (TAS) provides deep insights into the dynamics of interfacial hot carrier (HC) extraction. Fig. 3d–g presents the typical pseudo-color TA maps of perovskite films coated with different HTMs under 540 nm excitation with a low pump fluence of 0.82 μJ cm^{-2}. All spectra are dominated by a negative photobleaching (PB) peak centered around 770 nm, which is attributed to band-edge carrier state filling.[40] The corresponding normalized transient absorption spectral profiles from 0.4 to 2 ps exhibit a broadening of the PB signal in the high-energy region for all samples (Fig. 3h–k), which originates from the distribution of hot carriers.[41] To quantitatively analyze the HC cooling process, we extracted the carrier temperature (T_c) as a function of time (Fig. 3l), which is determined by fitting the high-energy tail with a Maxwell–Boltzmann distribution function. The calculation method is detailed in the SI. To obtain the specific cooling time (τ_{co}), all $T_c(t)$ curves were fitted using a single exponential function. Notably, the perovskite film coated with 2MPA exhibits the shortest cooling time of 149.4 fs, followed by 3MPA (178.1 fs), Spiro (220.8 fs), and MPA (232.5 fs). Herein, the decay of T_c is predominantly governed by carrier scattering with longitudinal-optical (LO) phonons within the perovskite film, as well as the interfacial carrier extraction from the perovskite into the HTM.[42] As our modifications were made to HTMs, the most rapid cooling time of 2MPA evidences more efficient hot carrier extraction at the perovskite/HTM interface, which can be attributed to its superior passivation capability and interfacial energy level alignment.

Photovoltaic performance and device stability

The PSCs with the architecture of ITO/TiO_2/perovskite/HTLs/Au (Fig. S27) were fabricated to assess the application potential of the HTMs. As shown in Fig. 4a and Table 2, the 3MPA-based device delivers the highest power conversion efficiency (PCE) of 25.21% for a 0.1 cm^2 cell, with an open-circuit voltage (V_{oc}) of 1.182 V, short-circuit current density (J_{sc}) of 26.28 mA cm^{-2}, and a fill factor (FF) of 81.13%, followed by 2MPA (24.86%), Spiro (23.94%), and MPA (20.89%) based devices. A statistical distribution of the photovoltaic parameters from 15 devices confirms the reproducibility of the PSCs (Fig. S28). To assess the applicability of 3MPA and 2MPA in large-area devices, 1 cm^2 solar cells were also fabricated, achieving power conversion efficiencies (PCEs) of 22.78% and 22.57% for 3MPA and 2MPA, respectively (Fig. S29 and Table S5). Maximum power point tracking (MPPT) under steady-state illumination for 300 s reveals stabilized efficiencies of 24.57%, 24.26%, 22.67% and 18.60% for 3MPA, 2MPA, Spiro and MPA, respectively (Fig. 4b). External quantum efficiency (EQE) spectra were integrated to obtain photocurrent values of 26.07 mA cm^{-2}, 25.89 mA cm^{-2}, 25.74 mA cm^{-2}, and 24.21 mA cm^{-2} for 3MPA, 2MPA, Spiro, and MPA, respectively (Fig. 4c), which matches well with the J_{sc} values derived from the J–V curves.

It can be seen that the device performance of PSCs based on the HTMs initially improves and then deteriorates with increasing number of carbazole units. To elucidate the underlying mechanism, we conducted a series of device physics characterizations. First, electrochemical impedance spectroscopy (EIS) was employed to investigate the recombination and charge transport characteristics. As exhibited in Fig. 4d and Table S6, Nyquist fitting plots reveal that the 3MPA-based device exhibits the lowest transport resistance (397 Ω), indicative of superior charge transport ability, while the 2MPA-based device exhibits the highest recombination resistance (49 KΩ), implying the lowest defect-assisted non-radiative recombination. Moreover, light-intensity-dependent V_{oc} measurements demonstrate that the 2MPA-based device has the lowest ideality factor of 1.44, followed by 3MPA (1.64), Spiro (1.72) and MPA (1.92) (Fig. 4e), suggesting reduced non-radiative recombination losses at the interface. Similarly, dark current measurements (Fig. S30) show that the 2MPA-based device exhibits the lowest leakage current, further confirming its superior defect passivation and recombination suppression. Mott–Schottky analysis in Fig. S31 reveals that the 3MPA-based device exhibits the highest built-in potential (V_{bi}) of 0.949 V, followed by 2MPA

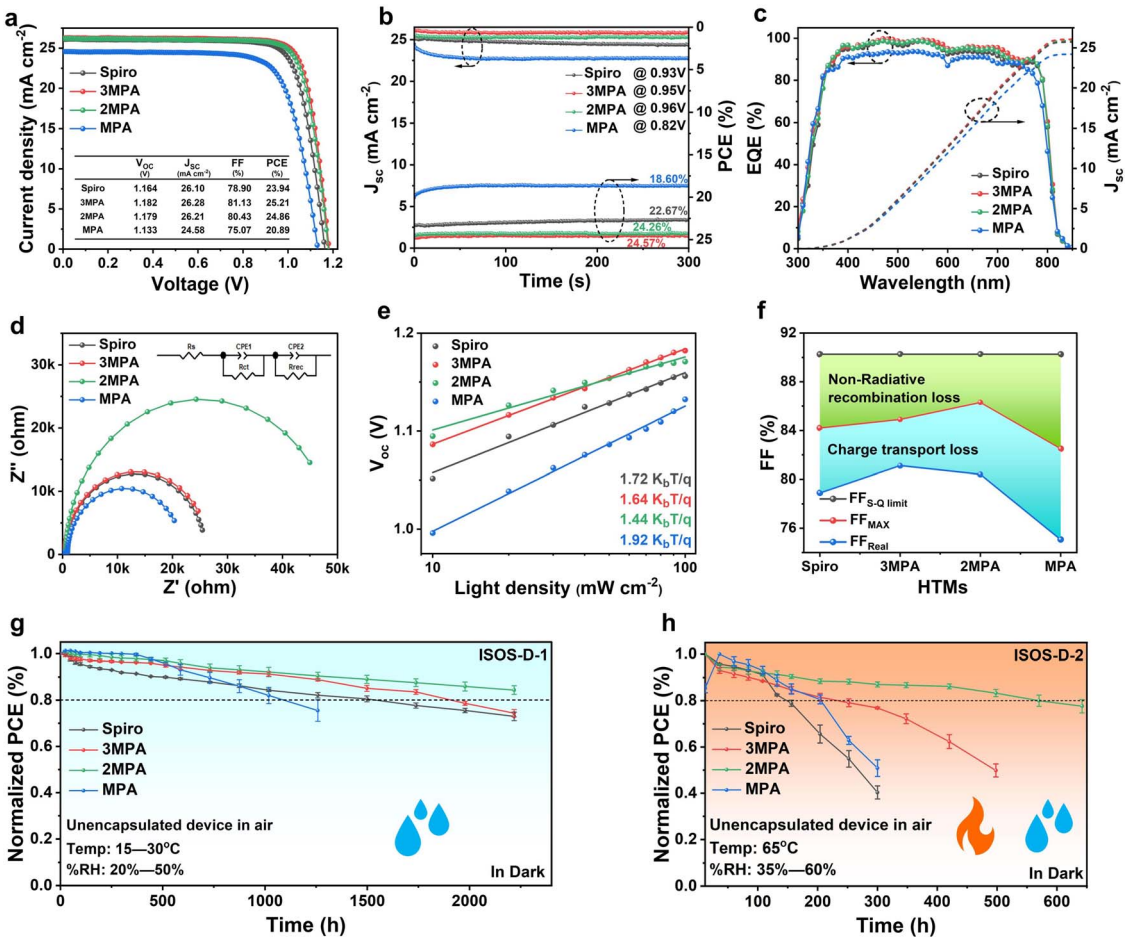

Fig. 4 Photovoltaic performance and stability of PSCs. (a) *J*–*V* characteristics of the champion devices. (b) MPP tracking for PSCs under continuous illumination. (c) EQE of the champion devices of PSCs based on different HTMs. (d) Nyquist plots of the impedance spectra with different HTMs. (e) Light intensity-dependent open-circuit voltage measurements. (f) The device FF limitation is composed of non-radiative loss and charge transport loss. (g) Storage stability of the unencapsulated PSCs based on different HTMs. (h) Thermal stability tests of the unencapsulated PSCs at 65 °C in air. The testing conditions conform to the ISOS-D-1 and ISOS-D-2 protocols.

(0.921 V), Spiro (0.886 V), and MPA (0.727 V), suggesting the stronger driving force for carrier separation and extraction, which is consistent with the measured V_{oc} values. According to the FF approximation equation,[20] the FF losses could be calculated as shown in Fig. 4f. Clearly, 2MPA demonstrates the lowest non-radiative recombination loss, indicating its strong defect passivation capacity and good interfacial contact. While 3MPA exhibits relatively larger recombination loss which is compensated with lower charge transport loss due to better film conductivity. To further quantify defect states, the space-charge-limited current (SCLC) method was employed. As shown in Fig. S32, the 2MPA-based device displays the lowest defect density (2.64×10^{15} cm^{-3}), followed by 3MPA (3.38×10^{15} cm^{-3}), Spiro (1.04×10^{16} cm^{-3}), and MPA (6.44×10^{16} cm^{-3})

Table 2 Champion photovoltaic performance of the devices based on different HTMs[a]

Compounds		J_{sc} (mA cm^{-2})	V_{oc} (V)	FF (%)	PCE (%)	PCE_{avg} (%)
Spiro	Forward	25.67	1.141	77.33	22.66	22.96 ± 0.78
	Reverse	26.10	1.164	78.90	23.94	
3MPA	Forward	26.00	1.167	80.77	24.51	24.63 ± 0.54
	Reverse	26.28	1.182	81.13	25.21	
2MPA	Forward	26.10	1.170	79.65	24.32	24.17 ± 0.36
	Reverse	26.21	1.179	80.43	24.86	
MPA	Forward	24.78	1.094	71.03	19.25	18.27 ± 1.53
	Reverse	24.58	1.133	75.07	20.89	

[a] Note: the average PCE is obtained from 15 PSC devices.

based devices. The significantly reduced defect densities in 2MPA- and 3MPA-based devices corroborate the suppressed non-radiative interfacial recombination losses.

Overall, it was found that the multiple properties of HTMs could be fine tuned through exquisitely regulating peripheral flexible diphenylamine and rigid carbazole fragments. Specifically, the introduction of more carbazole units can enhance the thermal stability and lower the HOMO level of HTMs as well as enabling more compact film morphology and strengthened passivation capacity. However, the negative impacts of more rigid carbazole units are the decreased solubility, reduced doping efficiency and conductivity of the HTMs. As a consequence, 3MPA and 2MPA can relatively balance the trade-off between various properties especially for film morphology and electrical properties of the HTMs, that is, 3MPA exhibits better electrical conductivity and lower charge transport losses while 2MPA shows superior film morphology and interfacial contact along with lower non-radiative recombination losses.

To systematically compare the economic costs of the HTMs from synthesis to device fabrication, we calculated both the precursor solution preparation costs and the single spin-coating costs for devices with different active areas (0.1 and 1 cm^2), as summarized in Tables S7 and S8. The cost analysis reveals that although the laboratory synthesis costs of 3MPA and MPA are higher than those of Spiro, their actual material consumption during spin-coating is significantly reduced, leading to lower practical material costs than for Spiro. Notably, the single spin-coating cost of 2MPA is substantially lower than that of the other HTMs due to its low synthetic cost and minimized material usage. This distinct advantage suggests that 2MPA is particularly promising for scaling up to large-area device fabrication and holds strong potential for cost-effective commercialization of PSCs.

Finally, the device stability was evaluated following the ISOS-D-1 and ISOS-D-2 protocols. The unencapsulated devices based on 2MPA can retain over 80% of their initial efficiency after more than 2000 h of storage under ISOS-D-1 conditions, outperforming those based on 3MPA (~1900 h), Spiro (~1500 h), and MPA (~1080 h) (Fig. 4g). Under ISOS-D-2 conditions (aging at 65 °C in ambient air without encapsulation), 2MPA-based devices can maintain over 80% efficiency after 550 h of continuous heating, significantly superior to those based on Spiro, 3MPA and MPA (Fig. 4h). It is worth noting that thermal aging promotes lithium-ion migration and enhances the interaction between lithium salts and MPA molecules, thereby improving the doping efficiency. This effect may account for the rise in efficiency observed in the initial stage of heating. Therefore, despite the higher PCE of 3MPA-based devices, 2MPA-based PSCs exhibit more excellent device stability. We speculate that 2MPA possessing more carbazole units has higher thermal stability and more compact film morphology than 3MPA, which contribute to higher T_g even in the doped state. As shown in Fig. S33, the T_g of the doped powder of the HTMs increases from 56.5 °C for Spiro to 78.3 °C for 2MPA along with the reduction for MPA (72.1 °C) which may be attributed to the higher doping concentration required for MPA and the increased heterogeneity in the doping system. Also, compared to 3MPA, 2MPA features better passivation capacity to inhibit interface degradation as well as a more hydrophobic surface to hinder moisture penetration (Fig. S34). Consequently, the storage and thermal stability can be remarkably enhanced for 2MPA-based PSCs.

Conclusions

In summary, we designed and explored a series of asymmetrical Spiro-type HTMs (3MPA, 2MPA and MPA) by exquisite modulation of diphenylamine and carbazole fragments. Compared to traditional HTM Spiro, the incorporation of carbazole units in HTMs led to enhanced thermal stability, lowered HOMO energy level, more compact film morphology and improved hole mobility in the pristine state as well as strengthened interactions with Pb^{2+} defects on the perovskite surface. However, excessive carbazole units (*e.g.* MPA and 4MCz) may decrease molecular solubility, undermine oxidative capacity, reduce doping efficiency and consequently impair the conductivity of the HTMs. Leveraging meticulous regulation of multiple properties of the HTMs, 3MPA and 2MPA based PSCs can deliver remarkably high PCEs of 25.21% and 24.86%, respectively, outperforming Spiro-based devices. Importantly, due to higher thermal stability, enhanced interfacial contact and a more hydrophobic surface, 2MPA based PSCs exhibit superior device stability under ISOS-D-1 and ISOS-D-2 conditions. This work provides comprehensive insights into the structure–property–performance correlations of Spiro-type HTMs and offers valuable design guidelines for the development of efficient and stable HTMs in PSCs.

Author contributions

M. A., Y. W. and W. H. supervised the project. M. A., D. W., D. C., Y. W., and W. H. conceived the idea and wrote the manuscript. X. W., W. J. *et al.* synthesized the materials, performed basic measurements, fabricated perovskite solar cells and performed characterization of devices. R. Z. performed femtosecond transient absorption spectroscopy. All authors discussed the results and assisted in the preparation of the manuscript.

Conflicts of interest

The authors declare no conflict of interest.

Data availability

The data that support the findings of this study are available from the corresponding authors upon reasonable request.

The supporting information (SI) includes detailed data and supporting materials, covering molecular synthesis procedures, device fabrication details, characterization methods and results, theoretical calculations, molecular structure confirmation spectra, fundamental material properties, and device performance characterizations, as presented in Fig. S1–S34 and Table S1–S8. See DOI: **https://doi.org/10.1039/d5sc05563f**.

Acknowledgements

The authors acknowledge the National Natural Science Foundation of China (No. 52203228 and 52002070), the Natural Science Foundation Project of Fujian Province (No. 2023J01527 and 2024J01304), and the Start-up funding from Fujian Normal University (No. Y072R024K13 and Y072R005K13).

Notes and references

1 Y. Shen, T. Zhang, G. Xu, J. A. Steele, X. Chen, W. Chen, G. Zheng, J. Li, B. Guo, H. Yang, Y. Wu, X. Lin, T. Alshahrani, W. Yin, J. Zhu, F. Wang, A. Amassian, X. Gao, X. Zhang, F. Gao, Y. Li and Y. Li, *Nature*, 2024, **635**, 882–889.
2 H. Chen, C. Liu, J. Xu, A. Maxwell, W. Zhou, Y. Yang, Q. Zhou, A. S. R. Bati, H. Wan, Z. Wang, L. Zeng, J. Wang, P. Serles, Y. Liu, S. Teale, Y. Liu, M. I. Saidaminov, M. Li, N. Rolston, S. Hoogland, T. Filleter, M. G. Kanatzidis, B. Chen, Z. Ning and E. H. Sargent, *Science*, 2024, **384**, 189–193.
3 Q. Li, H. Liu, C.-H. Hou, H. Yan, S. Li, P. Chen, H. Xu, W.-Y. Yu, Y. Zhao, Y. Sui, Q. Zhong, Y. Ji, J.-J. Shyue, S. Jia, B. Yang, P. Tang, Q. Gong, L. Zhao and R. Zhu, *Nat. Energy*, 2024, **9**, 1506–1516.
4 Y. Huang, K. Yan, X. Wang, B. Li, B. Niu, M. Yan, Z. Shen, K. Zhou, Y. Fang, X. Yu, H. Chen, L. Zhang and C. Li, *Adv. Mater.*, 2024, **36**, 2408101.
5 P. Ganesan, M. K. Nazeeruddin and P. Gao, *J. Mater. Chem. A*, 2024, **12**, 12983–13058.
6 Z. Hawash, L. K. Ono and Y. Qi, *Adv. Mater. Interfaces*, 2018, **5**, 1700623.
7 Y. Liu, H. Zhang, Y. Zhang, B. Xu, L. Liu, G. Chen, C. Im and W. Tian, *J. Mater. Chem. A*, 2018, **6**, 7922–7932.
8 F. M. Rombach, S. A. Haque and T. J. Macdonald, *Energy Environ. Sci.*, 2021, **14**, 5161–5190.
9 Y. Shen, K. Deng and L. Li, *Small Methods*, 2022, **6**, 2200757.
10 A. K. Jena, Y. Numata, M. Ikegami and T. Miyasaka, *J. Mater. Chem. A*, 2018, **6**, 2219–2230.
11 S.-Y. Jeong, H.-S. Kim and N.-G. Park, *ACS Appl. Mater. Interfaces*, 2022, **14**, 34220–34227.
12 S. N. Habisreutinger, N. K. Noel, H. J. Snaith and R. J. Nicholas, *Adv. Energy Mater.*, 2017, **7**, 1601079.
13 S. Wang, M. Sina, P. Parikh, T. Uekert, B. Shahbazian, A. Devaraj and Y. S. Meng, *Nano Lett.*, 2016, **16**, 5594–5600.
14 X. Sun, F. Wu, C. Zhong, L. Zhu and Z. Li, *Chem. Sci.*, 2019, **10**, 6899–6907.
15 Z. Xia, X. Feng, T. Wu, W. Zhang, C. Chen, L. Wang, W. Zhang, H. Wang, Y. Tian, Y. Hua, H. Chen and M. Cheng, *Adv. Funct. Mater.*, 2024, **34**, 2408423.
16 Q. Cheng, H. Chen, F. Yang, Z. Chen, W. Chen, H. Yang, Y. Shen, X. Ou, Y. Wu, Y. Li and Y. Li, *Angew. Chem., Int. Ed.*, 2022, **61**, e202210613.
17 Y. Wang, W. Chen, L. Wang, B. Tu, T. Chen, B. Liu, K. Yang, C. W. Koh, X. Zhang, H. Sun, G. Chen, X. Feng, H. Y. Woo, A. B. Djurišić, Z. He and X. Guo, *Adv. Mater.*, 2019, **31**, 1902781.
18 G. Xie, J. Wang, S. Yin, A. Liang, W. Wang, Z. Chen, C. Feng, J. Yu, X. Liao, Y. Fu, Q. Xue, Y. Min, X. Lu and Y. Chen, *Angew. Chem., Int. Ed.*, 2024, **63**, e202403083.
19 Y. Guo, L. He, J. Guo, Y. Guo, F. Zhang, L. Wang, H. Yang, C. Xiao, Y. Liu, Y. Chen, Z. Yao and L. Sun, *Angew. Chem., Int. Ed.*, 2022, **61**, e202114341.
20 W. Chen, Y. Wang, B. Liu, Y. Gao, Z. Wu, Y. Shi, Y. Tang, K. Yang, Y. Zhang, W. Sun, X. Feng, F. Laquai, H. Y. Woo, A. B. Djurišić, X. Guo and Z. He, *Sci. China Chem.*, 2021, **64**, 41–51.
21 Q. Cheng, H. Chen, W. Chen, J. Ding, Z. Chen, Y. Shen, X. Wu, Y. Wu, Y. Li and Y. Li, *Angew. Chem., Int. Ed.*, 2023, **62**, e202312231.
22 H. Choi, J. Lee, H. Kim, J. Kim, T. Park and S. Song, *ACS Sustainable Chem. Eng.*, 2022, **10**, 14948–14954.
23 H. Zhou, W. Wang, Y. Duan, R. Sun, Y. Li, Z. Xie, D. Xu, M. Wu, Y. Wang, H. Li, Q. Fan, Y. Peng, Y. Yao, C. Liao, Q. Peng, S. Liu and Z. Liu, *Angew. Chem., Int. Ed.*, 2024, **63**, e202403068.
24 J. Zhu, X. Huang, Y. Luo, W. Jiao, Y. Xu, J. Wang, Z. Gao, K. Wei, T. Ma, J. You, J. Jin, S. Wu, Z. Zhang, W. Liang, Y. Wang, S. Ren, C. Wang, C. Chen, J. Zhang and D. Zhao, *Nat. Commun.*, 2025, **16**, 240.
25 N. J. Jeon, H. Na, E. H. Jung, T.-Y. Yang, Y. G. Lee, G. Kim, H.-W. Shin, S. Il Seok, J. Lee and J. Seo, *Nat. Energy*, 2018, **3**, 682–689.
26 M. Jeong, I. W. Choi, E. M. Go, Y. Cho, M. Kim, B. Lee, S. Jeong, Y. Jo, H. W. Choi, J. Lee, J.-H. Bae, S. K. Kwak, D. S. Kim and C. Yang, *Science*, 2020, **369**, 1615–1620.
27 M. Jeong, I. W. Choi, K. Yim, S. Jeong, M. Kim, S. J. Choi, Y. Cho, J.-H. An, H.-B. Kim, Y. Jo, S.-H. Kang, J.-H. Bae, C.-W. Lee, D. S. Kim and C. Yang, *Nat. Photon.*, 2022, **16**, 119–125.
28 X. Liu, B. Zheng, L. Shi, S. Zhou, J. Xu, Z. Liu, J. S. Yun, E. Choi, M. Zhang, Y. Lv, W.-H. Zhang, J. Huang, C. Li, K. Sun, J. Seidel, M. He, J. Peng, X. Hao and M. Green, *Nat. Photon.*, 2023, **17**, 96–105.
29 T. Zhang, F. Wang, H.-B. Kim, I.-W. Choi, C. Wang, E. Cho, R. Konefal, Y. Puttisong, K. Terado, L. Kobera, M. Chen, M. Yang, S. Bai, B. Yang, J. Suo, S.-C. Yang, X. Liu, F. Fu, H. Yoshida, W. M. Chen, J. Brus, V. Coropceanu, A. Hagfeldt, J.-L. Brédas, M. Fahlman, D. S. Kim, Z. Hu and F. Gao, *Science*, 2022, **377**, 495–501.
30 T. Zhao, X. Jin, M.-H. Li, J. Li, S. Wang, Z. Zhang, P. Sun, S. Lin, Q. Chen, J.-S. Hu, Y. Li and Y. Jiang, *J. Am. Chem. Soc.*, 2024, **146**, 30893–30900.
31 J. Zhou, L. Tan, Y. Liu, H. Li, X. Liu, M. Li, S. Wang, Y. Zhang, C. Jiang, R. Hua, W. Tress, S. Meloni and C. Yi, *Joule*, 2024, **8**, 1691–1706.
32 X. Wang, M. Wang, Z. Zhang, D. Wei, S. Cai, Y. Li, R. Zhang, L. Zhang, R. Zhang, C. Zhu, X. Huang, F. Gao, P. Gao, Y. Wang and W. Huang, *Research*, 2024, **7**, 0332.
33 N. J. Jeon, H. G. Lee, Y. C. Kim, J. Seo, J. H. Noh, J. Lee and S. I. Seok, *J. Am. Chem. Soc.*, 2014, **136**, 7837–7840.
34 S. A. Ok, B. Jo, S. Somasundaram, H. J. Woo, D. W. Lee, Z. Li, B.-G. Kim, J. H. Kim, Y. J. Song, T. K. Ahn, S. Park and H. J. Park, *Nat. Commun.*, 2018, **9**, 4537.

35 W. Zhang, L. Wang, Y. Guo, B. Zhang, V. Leandri, B. Xu, Z. Li, J. M. Gardner, L. Sun and L. Kloo, *Chem. Commun.*, 2020, **56**, 1589–1592.
36 Y. Wang, S. Wang, N. Zhao, B. Gao, S. Shao, J. Ding, L. Wang, X. Jing and F. Wang, *Polym. Chem.*, 2015, **6**, 1180–1191.
37 R. L. Forward, K. Y. Chen, D. M. Weekes, D. J. Dvorak, Y. Cao and C. P. Berlinguette, *ACS Energy Lett.*, 2019, **4**, 2547–2551.
38 X. Huang, Z. Zhang, Y. Li, L. Zhang, C. Wang, L. Liang, C. Li, C. Liu, Z. Zhou, R. Zhang, Y. Wang, M. An, Y. Wang and P. Gao, *J. Energy Chem.*, 2025, **104**, 422–430.
39 Y. Wang, W. Chen, L. Wang, B. Tu, T. Chen, B. Liu, K. Yang, C. W. Koh, X. Zhang, H. Sun, G. Chen, X. Feng, H. Y. Woo, A. B. Djurišić, Z. He and X. Guo, *Adv. Mater.*, 2019, **31**, 1902781.
40 J. Fu, Q. Xu, G. Han, B. Wu, C. H. A. Huan, M. L. Leek and T. C. Sum, *Nat. Commun.*, 2017, **8**, 1300.
41 Y. Yang, D. P. Ostrowski, R. M. France, K. Zhu, J. Van De Lagemaat, J. M. Luther and M. C. Beard, *Nat. Photon.*, 2016, **10**, 53–59.
42 M. Li, S. Bhaumik, T. W. Goh, M. S. Kumar, N. Yantara, M. Grätzel, S. Mhaisalkar, N. Mathews and T. C. Sum, *Nat. Commun.*, 2017, **8**, 14350.